SUPPLEMENTARY INFORMATION

Part 1: CDA Data and Laboratory Experiments

CDA data

The dataset was obtained between October 10, 2004 and December 25, 2005 during several spacecraft crossings of the E ring plane. From a total of almost 3000 spectra, we used 1676 well resolved spectra for our analysis. The characteristics of Na-rich and Na-poor spectra can also be observed in spectra recorded between 2006 and 2008, although they are not subject to the statistical evaluation in this work.

Table S1: Detection statistics of the data set.

	Type I (Na-poor)	**Type II** (Na-poor)	**Type III** (Na-rich)
Composition	Almost pure water ice, Na + K traces	Water ice with organic compounds or silicates, Na + K traces	Water ice containing abundant Na-salts
Number	2,247* (1231)	504 (338)	167 (107)
With Na mass lines	93%	90%	100%
Na/H_2O**	$5x10^{-5(\pm1)} – 5x10^{-8(\pm1)}$	$5x10^{-5(\pm1)} – 5x10^{-8(\pm1)}$	$10^{-2} – 10^{-3}$
# avg. ions / spectrum	70,000	100,000	110,000

For determination of the Na frequency, Na/H_2O, and average Ions only the well resolved + high quality spectra were used (number in brackets). 47 spectra (2.8%) showed pronounced characteristics of both Na-poor and Na-rich spectra.

* In low quality spectra, Type I is always overestimated.

** For spectra with Na mass lines above the detection limit. The ratio determination considers the ionisation probability. The comparison of CDA spectra with our laboratory laser spectra provided more precise numbers ($10^{-7} – 10^{-8}$), which are at the lower end of this estimate.

CDA's[14] minimum detectable Na^+/H_3O^+ ratio (cationic species) lies between $5x10^{-5}$ and 10^{-3}, varying with the total ion yield of individual spectra. As calibration experiments confirm[30,31], due to its low ionization energy, the ionization probability of sodium at the impact is several orders of magnitude higher than that of water. Thus, to translate the ion count into an abundance of neutral components in the grain, this has to be taken into account. Here, we assume an ionization probability of $Na/H_2O = 10^{-3(\pm1)}$ during an impact onto the CDA target. This leads to a detection limit of $Na/H_2O = 5x10^{-8(\pm1)}$ to $10^{-6(\pm1)}$. The ion ratios for individual Type I and II spectra were determined by the amplitudes of the respective ions and their cluster-species. To determine the Na/H_2O ratio in the ice grain, we then applied the normalization factor for ionization probability which also determines the quantitative error of the measurement.

Ambiguity of mass lines

The CDA spectral peaks at 81 and 121 u which we assign to $(NaCl)Na^+$ and $(NaOH)(NaCl)Na^+$ respectively, are in principle also in agreement with $(NaOH)(H_2O)Na^+$ and $(NaOH)_2(H_2O)Na^+$. Although the parallel formation of the latter species is likely[18], the high resolution laboratory experiments confirm that NaCl species dominate in the concentration regime considered here. The two isotopes of chlorine produce double peaks (81+83 u and 121+123 u) with the expected isotopic ratio of 3:1 (Fig. 2b).

The ions of the CDA rhodium target material Rh^+ and the hydroxyl-cluster ion $(NaOH)_2Na^+$ both have a mass of 103 u and are thus indistinguishable in sodium rich Type III spectra. However, there is no such interference in Type I and II spectra (Fig.1). From there, it is known that in most cases the impact energy densities of E ring grains are not sufficient for the abundant formation of Rh^+ in the impact speed regime relevant to the dataset[9]. In contrast, Type III spectra show a much more pronounced 103 u signal and thus the mass line is mostly due to $(NaOH)_2Na^+$. This conclusion is confirmed by the laboratory laser experiments, which roughly reproduce the relative abundances of $(NaOH)Na^+$, $(NaOH)_2Na^+$, and $(NaOH)_3Na^+$ of CDA Type III spectra (Figs. 1 and 2).

Na contamination of the CDA detector target

In previous publications a Na contamination of CDA's rhodium target has been reported. Meanwhile this has been subject to a thorough investigation and could be quantified more precisely. A dominant contaminant origin of the frequent Na^+ mass lines in Type I and II spectra can now be ruled out. An analysis of Saturnian stream particle spectra and other non-E ring spectra, yield frequencies of Na mass lines much lower (< 30%) than even in Na-poor E ring grains (> 90%). Details about this and other investigations of the CDA contamination-state are summarized in an extensive report[19].

Concept of liquid beam laser dispersion and impact dispersion

To constrain further our measurements of Saturn's E ring both qualitatively and quantitatively, spectra from different Na^+ salt concentrations have been measured in laboratory experiments. These high-resolution spectra have enabled us to interpret the lower resolution CDA spectra in several cases and helped to narrow down the quantitative results. Laser ionisation is a standard technique to simulate the impact process with our instruments. In both cases (laser ionisation and impact ionisation) the material of interest (in this case water) is exposed to similar (and very high) energy densities and then the products are investigated via TOF spectroscopy.

Due to the very high energy density (as compared to the cohesive energy density) applied to the analysed material, only the chemical composition, but not its physical state (liquid or solid) matters. Hence, the extreme environmental conditions at Saturn are of minor relevance to the process itself: Although the details of the ionization process and the phase of the particles in the laboratory experiment and at the CDA in space differ, we find that the laboratory experiments reproduce the CDA spectra very well, not only qualitatively, but with a surprising quantitative accuracy. Furthermore, mass spectra from experiments with projectiles shot onto water ice with traces of Na contamination[30] exhibited the same mass line pattern as our laser experiments (Fig. 1a).

Since a simple dispersion model (assuming aerosol type droplets near the surface of Enceladus' ocean) works well for the explanation of the Na-rich spectra of E ring grains, we anticipated that the dispersion process of a liquid salt solution (in vacuum)

should produce mass spectra similar to those measured with the CDA, providing a unique opportunity to complement the CDA spectra with laboratory spectra (Fig. S1). It is known that laser dispersion of a liquid micro beam (containing salts) generates charged water clusters quantitatively as a function of ion concentration[20,31-34]. Thus, we would expect to obtain spectra from such a process in the laboratory that are in agreement with the spectra measured with the CDA.

As an extension of our work we performed a series of experiments in which we studied dispersion of a liquid with VUV radiation (157nm) creating a plasma leading to plasma dispersion, in comparison to liquid dispersion with an IR laser. In both cases we observed rather similar features and an overall qualitative agreement between the mass spectra. The same type of comparison-experiments (VUV vs. IR) for dispersion of an ice sample, provide very similar spectra with almost perfect quantitative agreement.[35]

For the space born particles, dispersion of the liquid in the generation process and dispersion of the grains at the detector into fragments is expected to preserve the relative concentration and abundance of ions relative to water, as is the case for laser dispersion of liquids when compared with plasma dispersion and ice dispersion as outlined above. The current laser-based laboratory experiments therefore allow a reliable quantitative probe of the emission source.

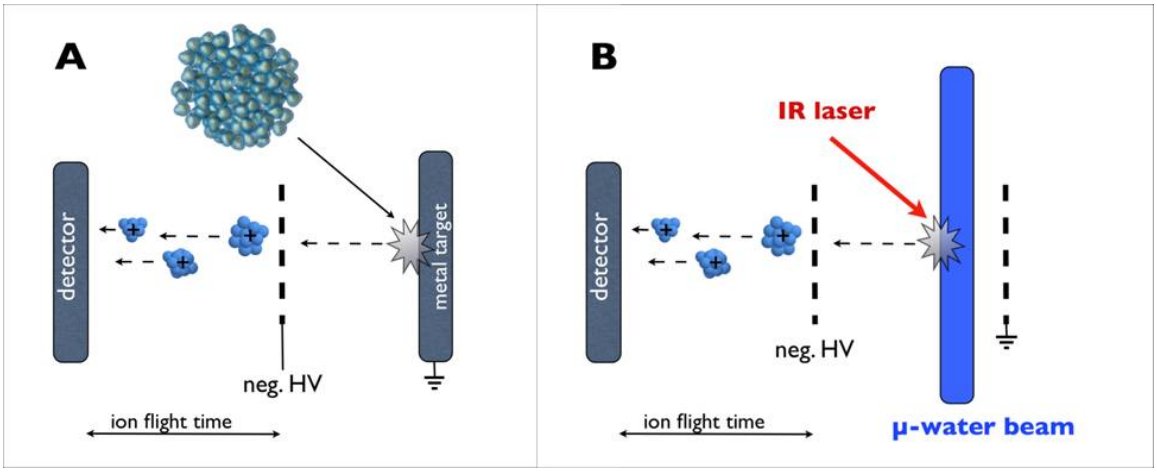

Figure S1: Comparison of CDA (A) and laboratory (B) measurements.

*The high velocity impact of a micron sized ice grain (**A**) and laser dispersion of a liquid water filament (**B**) cause a high degree of molecular and particle*

fragmentation. In both cases charged molecular fragment clusters are formed which can be investigated via Time-of-Flight mass spectrometry.

Experimental[20, 32-35]

A liquid beam with a diameter of about 14µm was formed by pumping doubly distilled water with a HPLC pump (model 300C, Gynkotek/Dionex, Germering, Germany) and at a flow rate of 250 µl/min through a quartz nozzle mounted on a three-axis manipulator in front of the mass spectrometer. Flow injection of the salt solutions was accomplished via a 100ml PEEK sample loop attached to an injection valve (model MX9925, Rheodyne, Rohnert Park, CA). The generated liquid jet consists of an intact ~3 mm long region which disintegrates into droplets further down.

The infrared laser beam (2.9µm, 2.5mJ/pulse) was generated by pumping an optical parametric oscillator (OPO) (GWU-Lasertechnik, Erfstadt, Germany) equipped with a $KNbO_3$ crystal with a 20Hz Nd:YAG-Laser (Quanta-Ray Indi series, Newport Corporation-Spectra Physics, Mountain View, CA). The IR beam was directed by gold mirrors, through a magnifying lens array, a focusing CaF_2 lens and a CaF_2 window onto the liquid target.

A reflectron Time of Flight mass spectrometer (Kaesdorf, Munich, Germany) operated in positive ion mode was used to sample about 200 spectra per delay time (12–29 µs) which were averaged and summed. NaCl p.a. and $NaHCO_3$ p.a., were purchased from Merck. All solutions were freshly prepared with double distilled H_2O before usage.

References

30 Timmermann, R. *Ladungsemmission bei Einschlägen schneller Mikroteilchen auf Wassereis*, *Ph.D thesis*, Heidelberg University, (1989).

31 Stübig, M. *New insights in impact ionization and in time-of-flight mass sectroscopy with micrometeroid detectors by improved impact simulations in the laboratory. Ph.D thesis*, Heidelberg University, (2002).

32 Charvat, A., Lugovoj, E., Faubel, M. and Abel, B. New design for a time-of-flight mass spectrometer with a liquid beam laser desorption ion source for the analysis of biomolecules. *Review of Scientific Instruments*, ***75*** **(5)**, 1209-1218 (2004).

33 Charvat, A., Stasicki, B. and Abel, B. Product screening of fast reactions in IR-laser-heated liquid water filaments in vacuum by mass spectrometry. *J. Phys. Chem. A,* ***110*** **(9)**, 3297-3306 (2006).

34 Charvat, A., Bögehold, A. and Abel, B. Time-resolved micro liquid desorption mass spectrometry: Mechanism, features, and kinetic applications. *Aust. J. Chem*., ***59***, 81-103 (2006).

35 A. Beinsen and B. Abel (2008), unpublished results.

Part 2
Modelling of the vent plumbing

1 Analysis of the quasi-equilibrium (steady state) approximation

In the analysis presented above it was implicitly assumed that the system is in thermodynamic equilibrium, which allows the application of the basic laws of equilibrium thermodynamics. On the other hand, it is known that a noticeable amount of water (about 100-300 kg/s) permanently leaves the satellite, leading to a continuing depletion of the water reservoir and enrichment in salinity. One must then ask whether the assumption of thermodynamic equilibrium is justified. To address this question we have to estimate the characteristic timescales involved in the processes.

The first timescale is related to the time of formation of a steady state vapour flux through the vents and, correspondingly, to the related time of a jet formation in the plume; both of them refer to the hydrodynamic timescale. The former may be estimated as $L_{\rm vent}/c$, where $L_{\rm vent}$ is the length of the vent (from the liquid surface to the outlet), $c \approx 500 m/s$ is the speed of sound in vapour. For values of $L_{\rm vent} \sim 10^2 - 10^5$ m we obtain for the first time scale $T_1 \sim 10^{-1} - 10^3\, s$, that is, tens of minutes as an upper limit. Similarly, the characteristic time for the formation of dust jets, $H_{\rm jet}/v_{\rm gas}$ ($H_{\rm jet} \sim 10^4 - 10^5$ m is the height of a jet, while $v_{\rm gas} \sim 10^2 - 10^3\, m/s$ is the gas speed in the plume), yields the same order of magnitude as T_1.

On the other hand, for the timescale related to the depletion of the water reservoir the following arguments are applied. For a wide range of plausible liquid volumes this timescale is fairly large. One can easily estimate the time T_2 it takes to double the mixing ratio $n(NaCl)/n(H_2O)$ in a liquid body of radius R, if the water evaporates with the rate γ, while the salt remains

$$T_2 = 3 \times 10^5 \text{years} \left[\frac{200 kg/s}{\gamma}\right] \left[\frac{R}{10 km}\right]^3 \qquad \text{(S1)}$$

where $\gamma = 200 kg/s$ is the current value of the evaporation rate. For a 10km radius liquid body (brine pocket) the timescale is 3×10^5 years, for a small local south polar ocean of 50km radius it is about 4×10^7 years and for a global ocean (200km equivalent radius) about 2.7×10^9 years. Hence, $T_2 \gg T_1$, which implies that our quasi-equilibrium approximation is indeed justified.

Since Enceladus' plume forms Saturn's E ring, a strict lower limit for the duration of the plume activity is given by the lifetime of the E ring grains, which is on the order of 100 years [36]. In this case we obtain from the above formula an equivalent radius of less than a kilometre

for the minimal size of the liquid reservoir, assuming an ongoing production at the currently observed rate. Smaller reservoirs would be exhausted before the E ring reached its present steady state with a balance of grain production in the plume and grain loss due to collisions with the embedded satellites and the A ring, as well as sputtering [36].

But in reality such a small duration of activity is highly unlikely. On the one hand the E ring must be sufficiently old (e.g. much older than the aforementioned 100 years) to modify the surface properties of its embedded satellites in the way as observed [37]. Namely, in [37] a compelling correlation is found between the albedos of the satellites (measured at true opposition) and their position in the ring, which is attributed to the pollution of the surfaces of the moons with fresh ice, produced by impacts of E ring grains. On the other hand, the duration of the plume activity is most likely related to the timescales of the thermal anomaly and the geological timescales of the formation of the south polar terrain. Although these timescales are poorly constrained, they most probably exceed 10^5 to 10^6 years, and we obtain from equation (S1) estimates for the *minimal* equivalent radius of the liquid volume of tens of kilometers.

We summarize our reasonings concerning the time scales as following:

a. The same timescale (i.e. T_2) applies for both the evolution of the liquid reservoir itself and a slow increase of the salinity of the reservoir by evaporation of water.
b. The precise nature of the heat source is still unknown. Thus, it is very possible that fresh salt-free ice is continuously melting. This would make the timescales T_2 obtained in equation (S1) above longer and could even lead to a strict steady state.
c. The steady state assumption we make for the processes of grain formation is not invalidated by a slow evolution (depletion) of a liquid reservoir, since, as has been shown above, $T_2 \gg T_1$. The condensation of grains, and the formation of droplets and freezing, as well as their escape through the plume, are fast processes, on timescales of minutes to hours at most.
d. For the interpretation of the data the relevant timescale is the lifetime of E ring grains, which is on the order of 100 years (see e.g. [36]). If the conditions on Enceladus are steady over such a time span, which should be fulfilled by an ample margin for a plausible liquid volume, then the spectra we obtain from the E ring grains are representative for this phase of Enceladus activity.
e. Changes in the level of activity of single plume sources on timescales of months or years (i.e. intermediate to the timescales of T_1 and T_2) would not affect our conclusions, as long as the average plume activity is steady over a time of 100 years, the lifetime of E ring grains.

2 The necessity of large liquid-gas interfaces

In this section we show that a small liquid-gas interface (i.e. at the site of evaporation) is not consistent with a steady outflow of gas and the continuous long term (years) activity of plume sources [38].

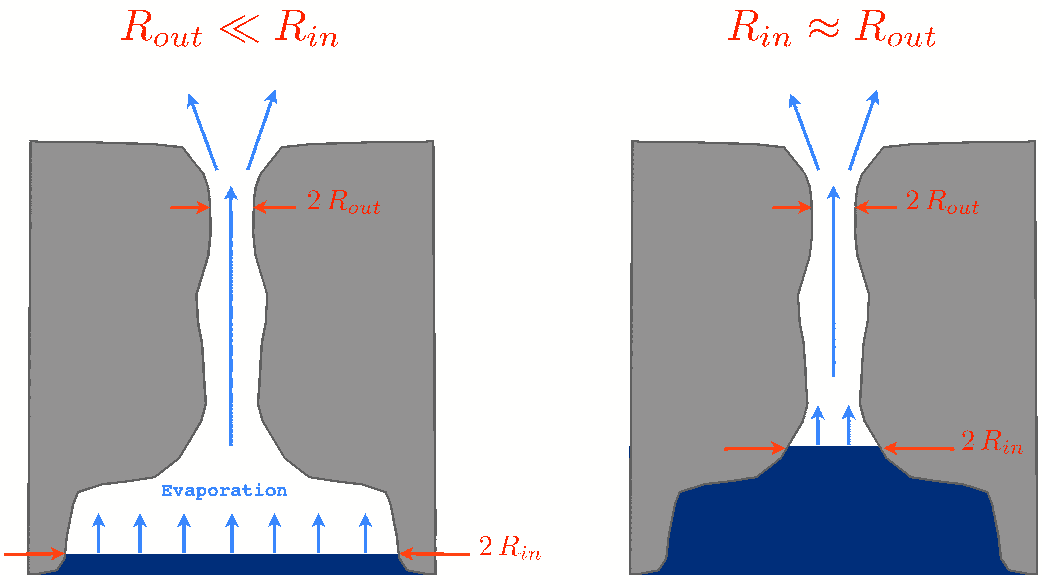

Fig. S2. A sketch of gas evaporating from subsurface liquid and flowing through cracks to vacuum. For the case of an outflow from a large gas reservoir (left panel) the theory outlined in [39] can be used, which is the base for the model proposed in [40]. For the case of a small liquid-gas interface (right panel) implausibly large temperature gradients in the liquid are needed to maintain a heat flux required to support the steady state gas evaporation.

We start by estimating the total cross-section A_v of all vents (outlets) on Enceladus contributing to the observed gas production rate of $\gamma \approx 200 kg/s$. We have

$$\gamma = A_v \, \rho_{gas} \, v_{gas} \tag{S2}$$

If we take for the gas speed a characteristic value of $v_{\rm gas} = 500 m/s$ [41, 42] and estimate the gas density from the equilibrium vapour pressure above liquid water at 273 K as $\rho_{\rm gas} \approx 4 \times 10^{-3} kg/m^3$ (which is the triple point density), we obtain active venting surface areas on the order of $100 m^2$. Taking into account the density drop in the vent, as well as the acceleration of the flow, vent models [40] suggest an actual value of

$$A_v \approx 200 m^2 \, . \tag{S3}$$

Such a relatively small total area of active venting surface is consistent with the observation of only isolated active plume sources on the tiger stripes [38].

If we define the characteristic radius of an isolated vent R_{out} near its outlet (Figure S2) then the mass outflow γ_1 of a single vent is given roughly by

$$\gamma_1 = \gamma \frac{\pi R_{out}^2}{A_v} \tag{S4}$$

This mass of gas is produced by evaporation from the liquid. Thus, with a latent heat of evaporation of $2.3 \times 10^6 J/kg$ for water we obtain for the heat flow through the liquid-gas interface

$$q_1 = 2.3 \times 10^6 \frac{J}{m^2\, s} \left[\frac{\gamma}{200\, kg/s}\right] \left[\frac{200\, m^2}{A_v}\right] \left(\frac{R_{out}}{R_{in}}\right)^2 \tag{S5}$$

where R_{in} defines the characteristic radius of the liquid-gas interface (Fig. S2).

For case of purely conductive heat transport we employ Fourier's law

$$q_1 = \kappa \nabla T\,. \tag{S6}$$

With a heat conductivity of $\kappa = 0.6 W\, K^{-1} m^{-1}$ for water we then arrive at an estimate for the temperature gradient in the liquid, which is in the steady state necessary to compensate for the loss due to the latent heat of evaporation

$$\nabla T \approx 4 \times 10^6 \frac{K}{m} \left[\frac{\gamma}{200\, kg/s}\right] \left[\frac{200\, m^2}{A_v}\right] \left(\frac{R_{out}}{R_{in}}\right)^2 \tag{S7}$$

This rough estimate immediately demonstrates the necessity of $R_{in} \gg R_{out}$, even an increase of A_v by orders of magnitude over the value estimated above would not help to avoid this conclusion. As we have argued in section 1 of this supplement the liquid body should have at least an equivalent radius of one kilometre and probably it is much larger. On the other hand the temperature difference across the liquid cannot exceed $100K$, so that a very conservative estimate of the maximum possible temperature gradient is given by $\Delta T/1000m = 0.1K/m^{\star}$. Using the characteristic values for A_v and γ given above, we then obtain from equation (S7) roughly the requirement

$$R_{in}^2 > 4 \times 10^7\, R_{out}^2\,. \tag{S8}$$

If there is convection in the liquid, the heat flow may be considerably larger. The ratio of convective to conductive heat flow is given by the Nusselt number Nu, so that

$$q_{convect} = \mathrm{Nu}\; q_{conduct} = \mathrm{Nu}\, \kappa \nabla T \tag{S9}$$

* Estimates have been made where the shift of water boiling temperature due to the hydrostatic pressure was taken into account. The maximum temperature gradient still safely remains below $0.1K/m$

For the classical Rayleigh-Bénard problem typical Nusselt numbers are between one and ten [43]. However, for large Rayleigh numbers Ra the Nusselt number can be considerably larger [44]. The Rayleigh number is given by

$$\mathrm{Ra} = g\frac{\alpha}{\kappa'\nu}\Delta T d^3 \tag{S10}$$

$$\approx 1.4\times 10^8 \left[\frac{\Delta T}{1K}\right]\left[\frac{d}{1m}\right]^3 \tag{S11}$$

with the gravitational acceleration $g \approx 0.1 m/s^2$, and the thermal expansion coefficient, heat diffusivity, kinematic viscosity ($\alpha = 2\times 10^{-4} 1/K$, $\kappa' = 1.4\times 10^{-7} m^2/s$, $\nu = 10^{-6} m^2/s$ [43]), and the temperature difference ΔT over the convective layer of thickness d. The latter quantities are poorly known. Still it is clear that the Rayleigh number easily assumes values as large as 10^{15} to 10^{20}. For an order of magnitude estimate of the possible influence of convection we use here the scaling reported in [44]

$$\mathrm{Nu} = 0.050\,\mathrm{Ra}^{1/3}, \tag{S12}$$

valid for the case of interest, when $\mathrm{Ra} > 10^{10}$ and $\mathrm{Pr} = \nu/\kappa' \simeq 7 > 1$ (Pr is the Prandtl number). In this regime (labeled IV_u in [44]) the dissipation in the bulk prevails over that in the boundary layer. It has to be noted however, that this estimate strictly applies only to convection in a plane-parallel layer without rotation. The actual geometry of the liquid body on Enceladus is unknown, and thus the boundary conditions, and it is not clear if there is convection at all. Nevertheless, the comparison to the Rayleigh-Bénard problem should give us an idea, how convection ultimately alters the magnitude of the heat flow. The above relation gives for the Nusselt number

$$\mathrm{Nu} \approx 26 \left[\frac{\Delta T}{1K}\right]^{1/3}\left[\frac{d}{1m}\right] \tag{S13}$$

and thus

$$q_{\mathrm{convect}} \approx 15 \left[\frac{\Delta T}{1K}\right]^{4/3}\frac{J}{m^2\,s} \tag{S14}$$

From the condition that all the heat transport is due to the convection, $q_{\mathrm{convect}} = q_1$, with q_1 given by Eq. (S5), we then obtain

$$R_{in} = 391.6\,R_{out}\left[\frac{1K}{\Delta T}\right]^{2/3} \tag{S15}$$

or

$$\left(\frac{R_{in}}{R_{out}}\right)^2 = \begin{cases} 1.5 \times 10^5, & \Delta T = 1K \\ 7 \times 10^4, & \Delta T = 10K \\ 3 \times 10^2, & \Delta T = 100K \end{cases} \tag{S16}$$

The quantity ΔT denotes the temperature difference across the convective layer (if any) which is unknown. Clearly, $\Delta T = 100K$ is implausibly large, and values on the order of a few Kelvins seem more realistic.

In consequence, the situation sketched in the right panel of Figure S2 cannot be a realistic model for Enceladus. It would work perhaps for a substantially lower mass production rate γ than the observed one. If such a configuration were realised on Enceladus, for instance by the sudden opening of a crack, the latent heat of evaporation would lead to rapid freezing of the liquid surface (see the discussion in [45]), i.e. the evaporation would be self-limiting, which is in contradiction to observations and the steady state assumption. Thus, if we accept the measured rate of mass production and the fact that the outflow is quasi-steady, then the left panel of Figure S2, with a large gas reservoir and large gas-liquid interface represents the only possible schematic model for the vents.

We conclude

a. In the case of a purely conductive heat transport in the liquid our estimates yield a total liquid surface of thousands of square kilometres (contributing by evaporation to gas flux), implying liquid under almost the whole southpolar terrain. In the case of a convective heat transport our estimates give liquid surfaces of a few to tens of square kilometres.
b. The actual geometry of the ice/liquid/gas interfaces is probably much more complicated than shown in the schematic drawing of Fig. S2. Each of the isolated plume sources identified in the imaging [38] might consist of many single vents. Moreover, different plume sources might connect to practically well separated parts of one big liquid reservoir, or even to different isolated reservoirs.
c. An increase of the salt concentration in the liquid near the (large) liquid-gas interface is implausible. Rapid mixing with the bulk water and even diffusion alone would be sufficient to rapidly smooth out such an enhanced salinity near the surface. In reality, since salty water is heavier, the highest salinity will establish at the bottom of the liquid, as is the case for terrestrial lakes, even when the gas evaporates from the surface.
d. Condensation, if any, of salt at the vent walls (thinking e.g. of rings of crystallized minerals on the container walls above a solution), will take place near the liquid-gas interface. Since this interface is large (Fig. S2), a clogging of the narrower vents — connecting the gas reservoir to vacuum — by salts is improbable.

3 Calculations leading to the theoretical curves in Figure 4 of the main paper

For a given number density n_l of undissolved NaCl molecules in liquid the number density of NaCl molecules n_v in vapour phase is given by

$$n_v = n_l \exp\left(\beta W_{\rm sol} + \beta W_{\rm d-ion}\right) \simeq n_l \exp\left(\beta W_{\rm sol}\right) , \tag{S17}$$

where $\beta = 1/k_B T$, k_B is the Boltzmann constant and T is temperature. The (main) first term in the exponent describes the difference in the free energy of the NaCl molecule in liquid and in the vapour phase due to the solvation, while the second term describes the interaction of the dipole molecule Na^+Cl^- with the positive Na^+ and negative Cl^- ions in liquid. For the range of parameters which are relevant for the present analysis, the second term in the exponent in Eq. (S17) may be neglected.

For the solvation energy $W_{\rm sol}$ we estimate, in section (3.1), an upper limit of -0.3 eV. Moreover, from simulations based on *ab initio* calculations and model potentials [46] solvation energies from -0.67 to -0.40 eV are found for a NaCl contact ion pair surrounded by one to ten water molecules, which should give a reasonable lower limit for $W_{\rm sol}$.

The concentration of ion pairs in the liquid, n_l, dependent on the total concentration of salt, we compute in section (3.2) from the Falkenhagen-Ebeling theory [47–49].

3.1 Estimate of the Solvation Energy

The solvation energy $W_{\rm sol}$ is generally a sum of two terms [50–52],

$$W_{\rm sol} = W_{\rm cav} + W_{\rm int} , \tag{S18}$$

where $W_{\rm cav}$ describes the cavity formation in the solution by the intrusion of a molecule and $W_{\rm int}$ refers to the electrostatic interaction between the solvent and solute.

3.1.1 Cavity Formation

For a spherical solute embedded in a solution comprised of spherical solvent particles $W_{\rm cav}$ is given by the *scaled particle* theory, e.g. [53, 54]. Here we apply the respective generalisation for hard aspherical particles [55]:

$$\beta W_{\rm cav} = -\log(1-\eta_w) + \left(\frac{3\eta_w}{1-\eta_w}\right)\frac{r_0}{r_w} + \left(\frac{3\eta_w}{1-\eta_w}\right)\frac{S_0}{S_w} \tag{S19}$$

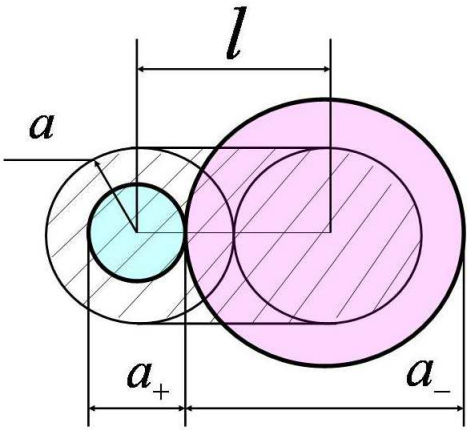

Fig. S3. The effective spherocylinder of length $l = (a_+ + a_-)/2$; the radius of the spherical caps is $a = l/2$. $a_+ = 2r_+$ and $a_- = 2r_-$ are the ion diameters.

$$+\frac{9}{2}\left(\frac{\eta_w}{1-\eta_w}\right)^2\left(\frac{r_0}{r_w}\right)^2+\beta PV_0\,,$$

where r_w is the solvent molecule radius (the radius of the water molecule in the case of interest), $\eta_w = 4\pi n_{\mathrm{wat,l}} r_w^3/3$ is the packing fraction of the solvent, $n_{\mathrm{wat,l}}$ the number density of water molecules in the liquid, $S_w = 4\pi r_w^2$ is the surface of the solvent molecule, r_0 is the average inverse curvature of the solute molecule [54], S_0 and V_0 are respectively its surface and volume and P is the pressure. For a spherical solute Eq. (S19) reduces to the standard result of the scaled particle theory, which was shown to be reasonably accurate, e.g. [50, 51]. Here we approximate a NaCl molecule (or an ion pair) by a spherocylinder of length $l = r_+ + r_-$ (r_+ and r_- are the radii of positive and negative ions) and with the radius of the spherical caps $a = (r_+ + r_-)/2$, equal to the average radius of the ions (Fig. S3). The corresponding quantities read for the spherocylinder [54],

$$\begin{aligned} r_0 &= a+\frac{1}{4}l = \frac{3}{4}(r_+ + r_-) = \frac{3}{4}d \\ S_0 &= 2\pi a(l+2a) = 2\pi d^2\,, \end{aligned} \tag{S20}$$

where we introduce $d = (r_+ + r_-)$.

3.1.2 Electrostatic Interaction Energy

The electrostatic interaction energy of a solute with the bulk water may be described as interaction with a dielectric continuum, if the discreteness of the medium and the dielectric saturation, e.g. [52, 56–58] are appropriately taken into account. The dielectric saturation implies that in very strong electric fields, where the interaction energy significantly exceeds the thermal energy, all dipoles (water molecules in our case) are completely oriented along the field. In this case the

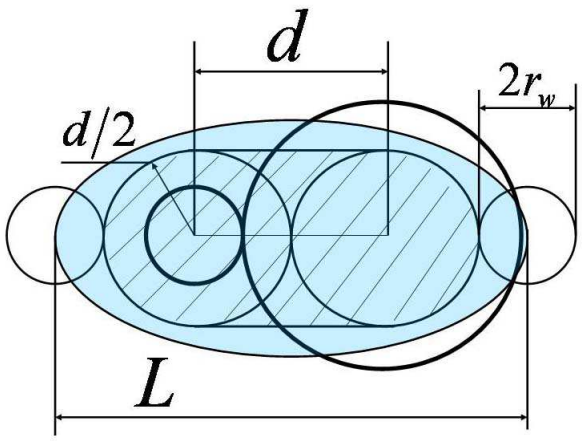

Fig. S4. The effective prolate spheroid representing an ion pair embedded in a dielectric continuum. The boundary of the continuum is placed at the centres of solvent molecules. The distance between the foci is $d = a_+ + a_-$ and the total length $L = 2d + 2r_w$, where r_w is the radius of the water molecule.

further increase of the field does not lead to an increase of polarisation. Hence, the polarisation (or equivalently the dielectric permittivity), that describes the response of the medium to the electric field becomes small in very strong fields.

The dielectric medium approximation corresponds to the zero-size limit of the solvent particles. The standard way to remedy the deficiency of the continuum approach is to reformulate the boundary conditions, that is, to shift the boundary of the dielectric medium to the centres of solvent particle in contact, e.g. [59, 60]. In other words, the dielectric continuum which surrounds a solute is assumed to start at the centres of solvent molecules. The dielectric saturation in this approach is also (at least partly) taken into account, since the zone of the most intensive electric field, where the dielectric constant drastically deviates from its bulk value, is excluded.

To describe the interaction of a dipole Na^+Cl^- with the dielectric continuum we apply the analytical expression obtained for a model of a dipolar molecule as a prolate spheroid (Fig. S4) with two opposite charges, $q_+ = q_- = q = e$, located at the foci of the spheroid [56]:

$$W_{\text{solv}} = \frac{2q^2}{d}\left(\frac{1}{\varepsilon} - 1\right) f_{\text{DS}}\left(\frac{L}{d}\right) \tag{S21}$$

$$f_{\text{DS}}(x) = \frac{x^2+1}{2x(x^2-1)} - \frac{x^2-1}{4x^2}\log\left(\frac{x+1}{x-1}\right), \tag{S22}$$

where $d = (r_+ + r_-)$ is, as before, the distance between the charges (i.e. between the foci) and L is the length of the spheroid, embedded in dielectric, and ε is the dielectric permittivity of water. From the geometry of the prolate spheroid and from the boundary conditions (the

dielectric starts at the centres of its molecules) it follows,

$$L = (a_+ + a_-) + 2r_w = 2d + 2r_w\,. \tag{S23}$$

3.2 Concentration of ion pairs in liquid

The formation of ion pairs in electrolyte solutions has been first described in the seminal work of Bjerrum and then many efforts have been made to improve this theory, e.g. [48,49,52]. One of the most successful continuum approaches to the ion pair formation is the Falkenhagen-Ebeling theory [47–49], which in present ("physical") notations reads [49],

$$\begin{aligned} n_l &= n_+^2 K(T) \exp(\beta\Delta\mu) \\ K(T) &= 4\pi d^3\, Q(b)\, e^b/b \\ Q(b) &= be^{-b} \int_1^\infty \left(e^{b/y} + e^{-b/y} - 2 - b^2/y^2\right) y^2 dy \end{aligned} \tag{S24}$$

where n_l is the number density of the ion pairs (undissolved NaCl molecules in liquid), $n_+ = n_-$ is the number density of ions, $d = r_+ + r_-$ (as previously), $b = l_B/d$, with the Bjerrum length

$$l_B = e^2/(\varepsilon k_B T) \tag{S25}$$

and the difference of the chemical potentials $\beta\Delta\mu$ is defined as

$$\beta\Delta\mu = -\frac{1}{32\pi}\frac{\kappa^3}{n_+}\left(\frac{1}{1+\kappa a_+} + \frac{1}{1+\kappa a_-}\right) \tag{S26}$$

where

$$\kappa = \sqrt{\frac{4\pi q^2 (n_+ + n_-)}{\varepsilon k_B T}} \tag{S27}$$

is the Debye-Huckel inverse screening length. The generalisation of the above expressions for the case of a few different ionic species with different charges is straightforward.

References

[36] A. Juhász and M. Horányi. Saturn's E ring: A Dynamical Approach. *Journal of Geophysical Research (Space Physics)*, 107:1–1, June 2002.

[37] A. Verbiscer, R. French, M. Showalter, and P. Helfenstein. Enceladus: Cosmic Graffiti Artist Caught in the Act. *Science*, 315:815, February 2007.

[38] J. N. Spitale and C. C. Porco. Association of the jets of Enceladus with the warmest regions on its south-polar fractures. *Nature*, 449:695–697, October 2007.

[39] L. D. Landau and E. M. Lifshitz. *Fluid Mechanics*. Pergamon, London, 1959.

[40] J. Schmidt, N. V. Brilliantov, F. Spahn, and S. Kempf. Formation of enceladus dust plume. *Nature*, 451:685, 2008.

[41] C. J. Hansen, L. Esposito, A. I. F. Stewart, J. Colwell, A. Hendrix, W. Pryor, D. Shemansky, and R. West. Enceladus' Water Vapor Plume. *Science*, 311:1422–1425, March 2006.

[42] C. J. Hansen, L. W. Esposito, A. I. F. Stewart, B. Meinke, B. Wallis, J. E. Colwell, A. R. Hendrix, K. Larsen, W. Pryor, and F. Tian. Water vapour jets inside the plume of gas leaving Enceladus. *Nature*, 456:477–479, November 2008.

[43] P. G. Drazin and W. H. Reid. Hydrodynamic stability. *NASA STI/Recon Technical Report A*, 82:17950, 1981.

[44] S. Grossmann and D. Lohse. Thermal Convection for Large Prandtl Numbers. *Physical Review Letters*, 86:3316–3319, April 2001.

[45] N. V. Brilliantov, J. Schmidt, and F. Spahn. Geysers of Enceladus: Quantitative analysis of qualitative models. *Planetary and Space Science*, 56:1596–1606, 2008.

[46] C. P. Petersen and M. S. Gordon. Solvation of Sodium Chloride: An Effective Fragment Study of $NaCl(H_2O)_n$. *J. Phys. Chem. A*, 103:4162–4166, 1999.

[47] H. Falkenhagen and W. Ebeling. In S. Petrucci, editor, *Ionic interactions*, New York, 1971. Academic Press.

[48] J. Barthel, W. Kunz, and H. Krienke. *Physical Chemistry of Electrolyte Solutions*. Springer, 1998.

[49] Y. Levin and M. E. Fisher. Criticality in the hard-sphere ionic fluid. *Physica A*, 225:164, 1996.

[50] M. Prevost, I. T. Oliveira, J.-P. Kocher, and S. J. Wodak. Free energy of cavity formation in liquid water and hexane. *J. Phys. Chem.*, 100:2738–2743, 1996.

[51] J. P. M. Postma, H. J. C. Berendsen, and J. R. Haak. Thermodynamics of cavity formation in water. *Faraday Symp. Chem. Soc.*, 17:55–67, 1982.

[52] J. O. M. Bockris, A. K. N. Reddy, and M. Gamboa-Aldeco. *Modern Electrochemistry*. Springer, 1998.

[53] R. A. Pierotti. A scaled particle theory of aqueous and nonaqueous solutions. *Chem. Rev.*, 76:717–726, 1976.

[54] J. A. Barker and D. Henderson. What is "liquid"? understanding the states of matter. *Rev. Mod. Phys.*, 48:587–671, 1976.

[55] T. Boublick. Statistical thermodynamics of convex molecule fluids. *Mol. Phys.*, 27:1415–1427, 1974.

[56] Yu. I. Kharkats. Calculation of the solvation energy of dipolar molecules. *J. Chem. Soc. Faraday Trans. II*, 70:1345 – 1347, 1974.

[57] K. J. Laidler and J. S. Muirhead-Gould. Continuous dielectric model for hydration of monoatomic ions. *Trans. Faraday Soc.*, 62:953–957, 1966.

[58] P. J. Stiles. Contribution from dielectric inhomogeneity to the free energy of ionic solvation. *Aust. J. Chem.*, 33:1389–1391, 1980.

[59] P. C. F. Pau, J. O. Berg, and W. C. McMillan. Application of stokes' law to ions in aqueous solution. *J. Phys. Chem.*, 94:2671 – 2679, 1990.

[60] N. V. Brilliantov, N. G. Vostrikova, and O. P. Revokatov. Role of electrical interactions in rotational motion of charged solute in polar solvents. *J. Phys. Chem. B*, 102:6299–6302, 1998.